Numerical simulation of piggyback pipelaying under current loadings

Chern Fong Lee [a], Guomin Ji [b], Marek Jan Janocha [a], Muk Chen Ong [a,*], Andreas Borsheim [a]

[a] Department of Mechanical and Structural Engineering and Materials Science, University of Stavanger, 4036, Stavanger, Norway
[b] Department of Manufacturing and Civil Engineering, Norwegian University of Science and Technology, 2815, Gjøvik, Norway

ARTICLE INFO

ABSTRACT

For piggyback pipelaying operations, current-induced force and its effect on the piggyback pipe have not been thoroughly studied. In the present study, an improved method in hydrodynamic load calculation and structural modelling is proposed to simulate the pipelaying of a piggyback pipeline. In order to obtain the mean drag and lift force coefficients for the piggyback pipeline subjected to different inflow angles, two-dimensional Computational Fluid Dynamics (CFD) simulations are performed by modelling the piggyback pipeline as two cylinders attached to each other without gap. Then, the acquired force coefficients are used to calculate the hydrodynamic loads through a user-defined function in OrcaFlex based on a cross-flow principle approach. The interaction between the pipeline and the piggyback cable is modelled using two types contact elements which are ring penetrator and non-penetrating contact. The present proposed method is compared with other two widely used engineering methods based on (1) the equivalent diameter and (2) two separate cylinders without accounting for hydrodynamic interaction, in terms of the top tension, and the bending moments at Hang-off Clamps (HOC) and sagbend of the pipeline. The comparison shows that the two widely used engineering methods are not always conservative in force and response predictions. Hence, it is important to consider the hydrodynamic and structural interactions between the piggyback cable and the pipeline. With different current directions, the bending moments at the HOC predicted by the present method vary from 40% lower to 100% higher than those predicted by the two widely used engineering methods.

1. Introduction

Submarine pipelines have been widely used to transport oil and gas between offshore and onshore production facilities. In deep waters, the combination of high-pressure flow and low ambient temperature results in the formation of hydrate that clogs up pipelines and reduces the volumetric flow rate of production fluid to subsea templates and offshore platforms; and this deteriorates production efficiency. Over the past two decades, the use of Direct Electrical Heating (DEH) cables has become increasingly popular to suppress the formation of hydrate. With the DEH system, an electrical cable is attached onto the main pipeline (i.e., piggybacking) while the continuous deployment of the pipeline bundle is taking place. The ways piggyback cable can be strapped onto the pipeline depend on cable protection systems which can be categorized into the Integrated Protection System (IPS) and the Mechanical Protection System

Nomenclature

C_d	Drag coefficient
C_l	Lift coefficient
C_p	Pressure coefficient
D_0	Diameter of the cylinder
D_1	Diameter of the pipeline
D_2	Diameter of the cable
$\vec{f}_{dn}$	Drag force normal to the pipeline axis per unit length
$\vec{f}_{lift}$	Lift force on the cylinder per unit length
G	Gap between large and small cylinders
K_C	Keulegan-Carpenter number
Re	Reynolds number
p_∞	Free stream flow pressure
p	Flow pressure
$\vec{U}_{inflow}$	Inflow velocity in 2D CFD simulation
f_x	Force component in the x-axis in 2D CFD simulation
f_y	Force component in the y-axis in 2D CFD simulation
$\vec{U}$	Current velocity
$\vec{U}_n$	Current velocity normal to the pipeline axis
$\vec{U}_{x'y'}$	Current velocity normal to the pipeline axis in OrcaFlex simulation
$U_{x'}$	Component of current velocity in local x'-axis in OrcaFlex simulation
$U_{y'}$	Component of current velocity in local y'-axis in OrcaFlex simulation
$U_{z'}$	Component of current velocity in local z'-axis in OrcaFlex simulation
θ	Direction of current $\vec{U}$ in global coordinate system in OrcaFlex simulation
φ	Angle between current velocity $\vec{U}$ and the local z'-axis in OrcaFlex simulation
α	Flow angle in 2D CFD simulation and flow angle between $\vec{U}_{x'y'}$ and local $x'-$ axis in $x'y'$-plane in OrcaFlex simulation
β	Pipeline inclination angle between z'-axis and the global xy-plane
γ	Pipeline angle of departure from vessel
ν	Kinematic viscosity
ρ_w	Fluid density

(MPS). The traditional MPS consists of holding blocks attached intermittently onto the external profile of the pipeline which offers protection by keeping the cable within its annulus. The holding blocks are assembled manually in-situ and strapped onto the pipeline during pipelaying operation. The IPS is a newer system that offers integrated protective layers providing continuous protection along
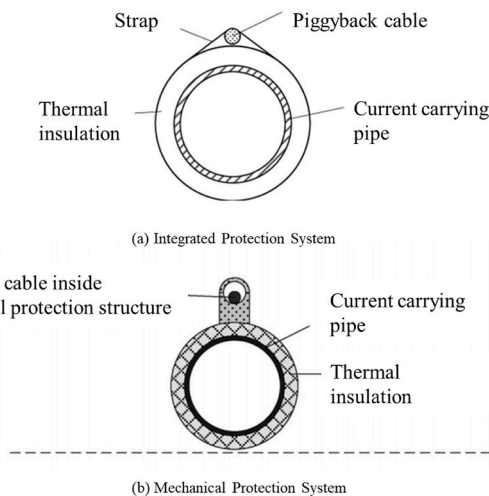

(a) Integrated Protection System

(b) Mechanical Protection System

Fig. 1. Comparison of different cable protection systems. Reproduced from Ref. [1].

the cable. The cable protected by the IPS can be directly strapped onto the production pipeline without holding blocks. Fig. 1 shows the cross-sectional comparison of the two protection systems. The IPS offers cost reduction and eliminates the need for the manual assembly of holding blocks. Therefore, the piggyback cable using the IPS is chosen for the present study. In a string of piggyback pipeline using the IPS, the cable is directly strapped into position via straps that are equally spaced along the pipeline. The friction between the straps, the cable and the pipeline prevents the cable from sliding axially along the flowline. It is therefore an industrial practice to provide overlength in between straps by snaking the piggyback cable to account for flowline expansion as illustrated in Fig. 2.

Pipelaying is a nonlinear problem involving large deflection, nonlinear contact between pipeline and seabed, as well as nonlinear external forces due to waves and currents. Nonlinear structural models are, therefore, commonly used to simulate pipelines' static and dynamic behaviours during pipelaying operations under environmental loadings. A critical area of concern is to establish pipelaying requirements under different operating conditions and to select the reasonable pipelaying vessels. Most of the published studies related to pipelaying analysis are dedicated to single pipelines. Lenci and Callegari [3] developed simple analytical models to simulate a J-lay operation. They extended the classical catenary equation to account for pipeline bending stiffness and the effect of seabed contact. Jensen et al. [4] derived a nonlinear finite element formulation of the elastic pipeline to simulate the dynamic behaviour of the pipeline catenary with integrated vessel dynamics and controls. Commercial software based on finite element method (FEM) such as RIFLEX, OrcaFlex, OFFPIPE, SIMLA and ABAQUS are typically used to perform analysis on pipelaying operations. A case study by Gong et al. [5] systematically outlined the methods of modelling the dynamic behaviour of S-lay pipeline using OrcaFlex. To date, limited studies onlaying piggyback pipelines have been published. Brany et al. [6] investigated the cable compressive strain at touch down point (TDP) and the compressive strain locally between adjacent straps with respect to the allocated cable overlength during installation.

It is a common engineering practice to approximate the hydrodynamic loads acting on piggyback pipeline configurations using an equivalent pipeline diameter approach. The piggyback pipeline is modelled as a single circular pipe with the physical properties of the pipeline and the equivalent pipeline diameter is taken as the sum of the diameters of pipeline and piggyback cable, as shown in Fig. 3. It is reasonable to believe that this approach is conservative in estimating hydrodynamic loads simply because it overestimates the projected area normal to the inflow directions. However, contrary to common understanding, the studies done by Kamarudin et al. [7] and Branković et al. [8] showed that the equivalent diameter approach is not always conservative. Kamarudin et al. [7] performed a computational fluid dynamic (CFD) analysis to investigate the influence of the smaller pipeline on the hydrodynamic characteristic of the main pipeline installed at the sea bottom. Their CFD result was benchmarked against the results calculated using the equivalent diameter approach. Theyfound that the equivalent diameter approach underestimated the total drag force and overestimated the total lift force on the pipeline bundle. The hydrodynamic properties of the piggyback bundle are strongly dependent on the orientation of the piggyback pipeline with respect to the incoming flow direction, and the use of an equivalent-diameter cylinder is unable to model the orientation-dependent properties of a piggyback pipeline. Branković et al. [8] performed physical tests to investigate the effect of current on a piggyback pipeline close to the seabed. Branković et al. [8] also reported an increase in drag force which was larger than that predicted using the equivalent-diameter approach. Janocha and Ong [9] performed a more realistic CFD analysis on highReynolds flow around two rigidly coupled cylindersby allowing the cylinders to vibrate in two degrees of freedom (DOFs). The predicted drag coefficients were found to be significantly higher than the results of a single stationary cylinder.

A realistic numerical method for predicting hydrodynamic loads on piggyback pipelines needs to take into account the interaction between pipelines and piggyback cable by capturing the flow behaviour around a two-cylinder configuration. Jakobsen and Sayer [10] demonstrated through experiments that the measured total drag forces on the piggyback configuration are higher than the summation of forces on two separate cylinders, and the increase is significant at high Keulegan-Capenter (K_C)numbers. This shows the significance of hydrodynamic interaction caused by the two cylinders being placed in close proximity. Drag forces on two side-by-side cylinders increase considerably as compared to a single cylinder in certain flow directions. At the same time, due to flow profile asymmetry (except for when the cylinders are placed in tandem in relation to the flow), there will be a non-zero time-averaged lift force.

The on-bottom stability of piggyback pipelines was studied in Refs. [7,8] while little attention has been given to the loading conditions on the piggyback pipeline catenary during pipelaying operations. Since the current velocity is significantly higher at the top
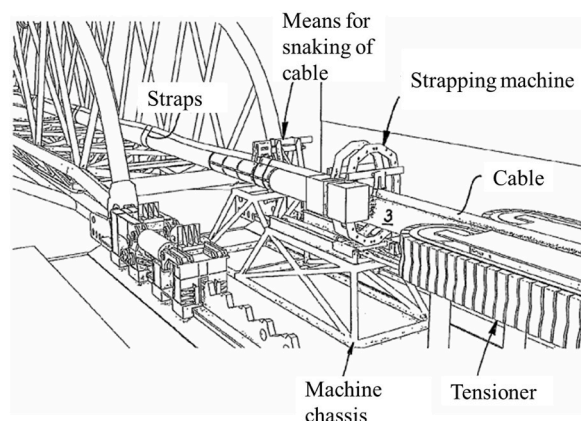

Fig. 2. Gentle snaking of cable to provide overlength during pipelaying operation. Reproduced from Ref. [2].
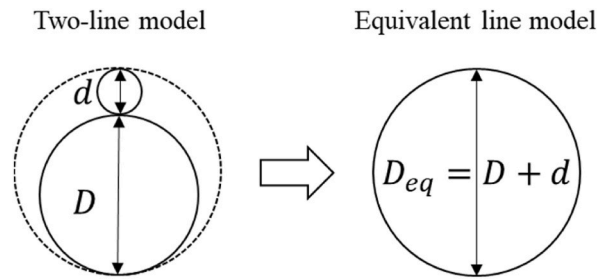
Fig. 3. Comparison of cross-sections between the equivalent diameter model and the two-line model.

half of the catenary, a change in force coefficient is bound to directly influence key operational parameters such as laying tension, pipeline layback and lay tower inclination. It is therefore of interest to accurately predict the force coefficients of the piggyback pipelines.

The present study investigates different approaches modelling the hydrodynamic and structural interactions of the piggyback pipeline during pipelaying operations. An improved model is proposed in the present study to specifically account for the interactions between the pipeline and piggyback cable in hydrodynamic and structural modelling. The hydrodynamic model of the piggyback pipeline is composed of two cylinders attached to each other in a two-dimensional (2D) configuration with varying orientation with respect to the free stream. A series of 2D Computational Fluid Dynamics (CFD) simulations is carried out to calculate the in-line (drag) and cross-flow (lift) force coefficients of the pipeline and piggyback cable, respectively, using an open-source CFD toolbox OpenFOAM [11]. The CFD-calculated force coefficients are then used to calculate hydrodynamic forces on the piggyback pipeline in OrcaFlex through a user-defined external function. OrcaFlex is a commercial 3D, nonlinear, time-domain finite element program which can be used to model a slender structure as discretized massless segments connected by nodes with concentrated mass [12]. The piggyback pipeline is modelled as two separate lines forming a bundle. The contact between the pipeline and piggyback cable is modelled using OrcaFlex's line contact model [12] which is described in detail in Section 3.3. The proposed model is compared with an engineering approach, in which the piggyback pipeline is modelled as one pipeline with an equivalent diameter, and an alternative approach, in which the pipeline and piggyback cable are modelled separately, and tabulated drag force coefficients of smooth single cylinders are used to calculate the hydrodynamic loads for the pipeline and piggyback cable, respectively.

The paper is organized as follows. Section 2 describes the investigated pipelaying configuration and the criteria of safe pipelaying operations. Section 3 presents the hydrodynamic and structural models used for the analyses. A detailed explanation on how hydrodynamic load calculation is implemented in OrcaFlex is provided. In Section 4, the flow around a piggyback pipeline configuration is analysed using the CFD method and the results are validated against published experimental and numerical data. Section 5 deals with the structural analysis of pipelaying operation incorporating the CFD-calculated force coefficients obtained in Section 4. The results obtained from three different modelling approaches are compared, and the importance of considering the interaction between the pipeline and the piggyback cable in the hydrodynamic and structural modelling is discussed. Finally, conclusion and recommendations concerning piggyback pipelaying operations are provided in Section 6.

2. Pipelaying configuration and parameters

2.1. Pipelaying configuration

Depending on the suspended pipeline configuration, pipelaying methods can be categorized into S-Lay, J-Lay and reel-lay. With the J-Lay method, the pipeline is lowered vertically from the pipelaying vessel forming a J-shaped pipeline catenary between the vessel and the seabed. For deep water pipelaying operations, the increase in suspended pipe length will increase the pipeline axial tension experienced at the pipelaying vessel. With a nearly vertical pipeline departure angle, the J-Lay method requires a lower axial tension at the tensioner, hence increasing the water depth for pipelaying operation. Many J-Lay vessels utilize Hang-off Clamps (HOC) to support the full weight of the suspended pipeline while pipe joints are being made up in the lay tower. The catenary top tension at HOC is measured by load cells. The angle with respect to the horizontal plane at which the pipeline is lowered is termed the departure angle (γ). During a pipelaying operation, the departure angle can be adjusted by changing the inclination of the lay tower to regulate loading on pipelines. As the departure angle of the J-Lay configuration is much greater than that of the S-Lay configuration, it results in a lower bending load at the region close to the HOC and tensioners. The J-Lay configuration is preferred for deep water pipelaying operations. In the present study, the pipelaying simulation with J-Lay configuration is performed for a water depth of 3000 m, as shown in Fig. 11.

2.2. Pipelaying requirements

The condition during a pipelaying operation is closely monitored using different measurement systems. The vessel position, TDP position, pipeline top axial tension and departure angle are to be monitored and kept within a predefined range to avoid overloading of pipeline during pipelaying operation. Pipeline top axial tension is one of the most significant parameters to consider as it sets the requirement for vessel and tensioner capacities.

According to DNVGL-ST-F101 [13], local buckling under environmental and operational loading should be checked for pipeline sections at free-span and HOC exit. It is important to ensure that the limit state criteria are satisfied in all critical areas. In the design process, the following three most important results from simulations are used to determine the allowable operation conditions:

- Pipeline top axial tension
- Pipeline bending moment at HOC exit
- Pipeline sagbend maximum bending moment

In the present study, they are used as parameters to compare the effect of different modelling methods, and position of those three parameters is shown in Fig. 11.

3. Proposed pipelaying model

3.1. Hydrodynamic model

The drag forces applied to pipeline are calculated using the cross-flow principle. The fluid velocity relative to the pipeline $\vec{U}$ is split into components $\vec{U}_n$ and U_z normal and parallel to the pipeline axis (i.e., consistent with OrcaFlex's definitions). The drag force normal to the pipeline axis per unit length $\vec{f}_{dn}$ is then given by:

$$\vec{f}_{dn} = \frac{1}{2}\rho_w C_d D_0 \vec{U}_n \left| \vec{U}_n \right|$$ (1)

where ρ_w is the fluid density, D_0 is the cylinder diameter, C_d is the drag coefficient. C_d varies with cross-section geometry and flow regime; and it is dependent on the local Reynolds number (Re) given by:

$$Re = \frac{\left| \vec{U}_n \right| D_0}{\nu}$$ (2)

where ν is the kinematic viscosity. The flow behaviour around the pipeline section undergoes drastic changes when the single cylinder configuration is replaced with a two-cylinder configuration.

3.2. Hydrodynamic coefficients for the two-cylinder configuration

In the present study, the turbulent flow past two circular cylinders of different diameters, shown in Fig. 4, is investigated numerically through 2D CFD simulations. The angle between the inflow velocity $\vec{U}_{inflow}$ ($\vec{U}_{inflow}$ in 2D is equal to $\vec{U}_n$ in 3D) and the line from the center of the piggyback cable (small cylinder) to the center of the pipeline (large cylinder) is defined as α. In CFD simulations, α is varied from $0°$ to $180°$ to the inflow. When $\alpha = 0°$, the small cylinder is located on the left side of the large cylinder. The small cylinder is mounted onto the large cylinder without gap. The diameter ratio of the large cylinder and the small cylinder (D/d) is set to a constant value of 3.92.

The main purpose of the CFD simulations is to provide more accurate drag coefficient values than the equivalent diameter method. 2D Unsteady Reynolds-averaged Navier-Stokes (RANS) simulations are proven to predict the drag of a cylinder reasonably well for $Re < 5 \times 10^5$, see e.g., Rosetti et al. [14]. Considering the computational cost and necessity to simulate a large number of flow cases (different flow velocities and different flow directions towards the piggyback pipeline), the 2D approach is selected. The turbulence model used in the present simulations, namely the k-ω SST model proposed by Menter et al. [15], can be integrated through the laminar
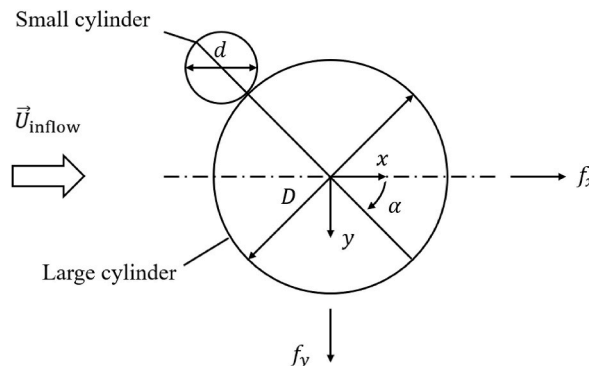

Fig. 4. Sketch of flow past a piggyback pipeline cross-section at flow direction α in 2D CFD simualtion.

sublayer without the necessity to use the wall functions. This model is known to perform well for the flows characterized by adverse pressure gradients and separation.

3.2.1. Governing equations

The Reynolds-averaged equations for conservation of mass and momentum of an incompressible flow is given by,

$$\frac{\partial u_i}{\partial x_i} = 0 \tag{3}$$

$$\frac{\partial u_i}{\partial t} + u_j \frac{\partial u_i}{\partial x_j} = -\frac{1}{\rho}\frac{\partial p}{\partial x_i} + \nu \frac{\partial^2 u_i}{\partial x_j \partial x_j} - \frac{\partial \overline{u_i' u_j'}}{\partial x_j} \tag{4}$$

where $i, j = 1, 2$. u_i is the mean velocity component in the i-th direction; t represents time; ρ is the fluid density; p is the pressure; ν is the kinematic viscosity. $\overline{u_i' u_j'}$ is the Reynolds stress component where u_i' and u_j' denote the fluctuating parts of the velocities. Governing equations are solved using OpenFOAM [11] employing the Finite Volume Method (FVM). The FVM integrates the scalar transport equation of potential over a control volume such that

$$\int_V \frac{\partial}{\partial t}(\rho \varphi) dV + \int_V \nabla \cdot (\rho \varphi u) dV = \int_V \nabla \cdot (\Gamma \nabla \varphi) dV + \int_V S_\varphi dV \tag{5}$$

where φ is the transported fluid property, V is the control volume, Γ is the diffusion coefficient and S_φ the source term. The shear stress transport (SST) $k - \omega$ turbulence model proposed by Menter [16] is used to determine the turbulent kinetic energy k and the turbulent viscosity ν_t In this paper, the equations for k and the specific dissipation rate of turbulent energy ω can be expressed as

$$\frac{\partial k}{\partial t} + u_j \frac{\partial k}{\partial x_j} = \tau_{ij} \frac{\partial u_i}{\partial x_j} - \beta^* k\omega + \frac{\partial}{\partial x_j}\left[(\nu + \sigma_k \nu_t)\frac{\partial k}{\partial x_j}\right] \tag{6}$$

$$\frac{\partial \omega}{\partial t} + u_j \frac{\partial \omega}{\partial x_j} = \alpha \Omega^2 - \beta^* \omega^2 + \frac{\partial}{\partial x_j}\left[(\nu + \sigma_\omega \nu_t)\frac{\partial \omega}{\partial x_j}\right] + 2(1 - F_1)\frac{\sigma_{\omega 2}}{\omega}\frac{\partial k}{\partial x_j}\frac{\partial \omega}{\partial x_j} \tag{7}$$

where τ_{ij} is the mean stress tensor and the turbulent viscosity ν_t can be evaluated given by,

$$\nu_t = \frac{a_1 k}{max(a_1 \omega, \Omega F_2)} \tag{8}$$

Vorticity magnitude W_{ij} and blending functions F_1 and F_2 can be expressed as follows,

$$a_1 = 0.31 \tag{9}$$

$$\Omega = \sqrt{2 W_{ij} W_{ij}} \tag{10}$$

$$W_{ij} = \frac{1}{2}\left(\frac{\partial u_i}{\partial x_j} - \frac{\partial u_j}{\partial x_i}\right) \tag{11}$$

$$F_1 = \tanh\left(arg_1^4\right) \tag{12}$$
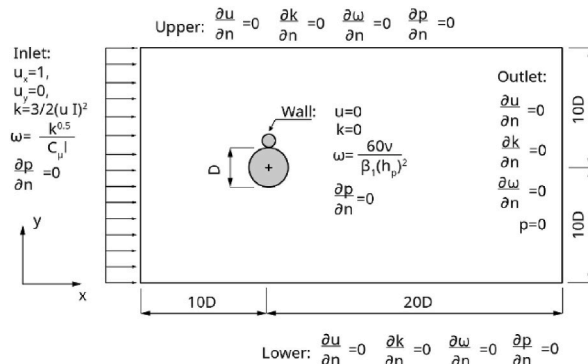
$$F_2 = \tanh\left(arg_2^2\right) \tag{13}$$

Fig. 5. CFD simulation domain and boundary conditions.

$$arg_1 = min\left[max\left(\frac{\sqrt{k}}{\beta^* \omega d_\omega}, \frac{500\nu}{d_\omega^2 \omega}\right), \frac{4\rho\sigma_{\omega 2}k}{CD_{k\omega}d_\omega^2}\right] \tag{14}$$

$$arg_2 = max\left(2\frac{\sqrt{k}}{\beta^* \omega d_\omega}, \frac{500\nu}{d_\omega^2 \omega}\right) \tag{15}$$

$$CD_{k\omega} = max\left(2\rho\sigma_{\omega 2}\frac{1}{\omega}\frac{\partial k}{\partial x_j}\frac{\partial \omega}{\partial x_j}, 10^{-20}\right) \tag{16}$$

The standard values of model constants used in the present study can be referred to Menter et al. [15].

3.2.2. Numerical method and boundary conditions

A rectangular computational domain, shown in Fig. 5, is established with dimensions of 30D (length) ×20D (width), in which D is the diameter of the large cylinder. The inlet boundary is located at a distance of 10D from the center of the larger cylinder. The upper and lower boundaries are located 10D away from the center of the larger cylinder. This ensures that the blockage is 5%, and the influence of the domain boundaries proximity on the results is negligible. Similar domain sizes were previously used in Janocha and Ong [9]. They used a 30D (length) ×10D (width) domain size to investigate the vortex-induced vibration (VIV) of piggyback pipelines near a horizontal plane wall in an upper transition flow regime. Palkin et al. [17] used a domain width of 20D for flow simulation around a circular cylinder at $Re = 1.4 \times 10^5$. At a downstream distance of 20D from the center of the larger cylinder, an outflow boundary condition with reference pressure set to zero is used. At the inlet, a uniform horizontal velocity profile is specified. Simulations are performed for inlet velocities of 1.5 m/s, 1.0 m/s and 0.5 m/s, respectively. Pressure-velocity coupling is solved using the PIMPLE algorithm. The implicit second-order Crank-Nicolson scheme is used for the time integration. The divergence and gradient terms are discretized using Gauss linear integration scheme. The Laplacian and surface normal gradients are discretized using Gauss linear integration with limited non-orthogonal correction. The present method is of second-order accuracy. Prior to the main parametric study, a series of simulations with varied mesh density are performed in order to assure that mesh independent solution is obtained. Based on the mesh convergence study, meshes with a total cell number of approximately 90000 are used in the parametric study. A typical computational grid used in the present study is shown in Fig. 6.

The present model is first validated against the experimental measurements by Tsutsui et al. [18]. The investigated geometry consisted of two cylinders of different diameters with a diameter ratio of $d/D = 0.45$ exposed to a uniform flow. The gap ratio between the two cylinders G/D is 0.0625. The Reynolds number based on the large cylinder diameter is $Re = 4.1 \times 10^4$ and the Reynolds number based on the small cylinder is $Re = 1.845 \times 10^4$. The same flow conditions were applied as used in the present CFD simulations. Fig. 7 shows the time-averaged pressure coefficient distribution on the surface of large and small cylinders for two representative cases with angular position $\alpha = 90°$ and $\alpha = 120°$. A good agreement is observed between the experimental measurements and the pressure coefficient C_p distribution predicted by the present CFD model. In the range of investigated Re, the contribution of the pressure component of drag is much larger than the contribution of the skin friction. Therefore, a good prediction of the C_p indicates that the present model can predict the drag force reasonably well.

The numerical simulation performed in this study is also verified against numerical simulation by Zhao et al. [19]. Zhao et al. [19] investigated flow around two cylinders with a diameter ratio D/d of 2.22 with a varying gap between two cylinders ($Re = 5 \times 10^4$ for large cylinder and $Re = 2.5 \times 10^4$ for small cylinder). The numerical result using the smallest gap ratio of $G/D = 0.05$ is compared with the present study. It can be shown that the numerical results in the present study agree reasonably well with the finding presented by Zhao et al. [19] shown in Figs. 14 and 15.
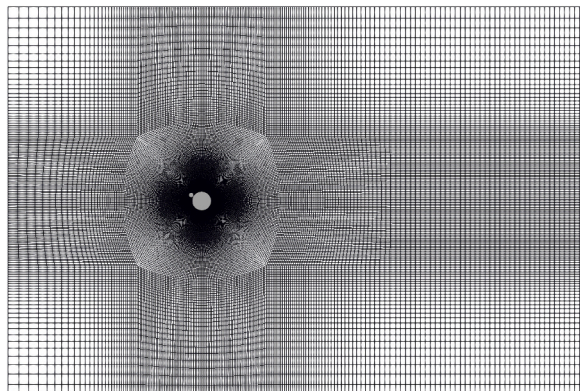

Fig. 6. Overview of a computational grid topology used in the present study.

(a)
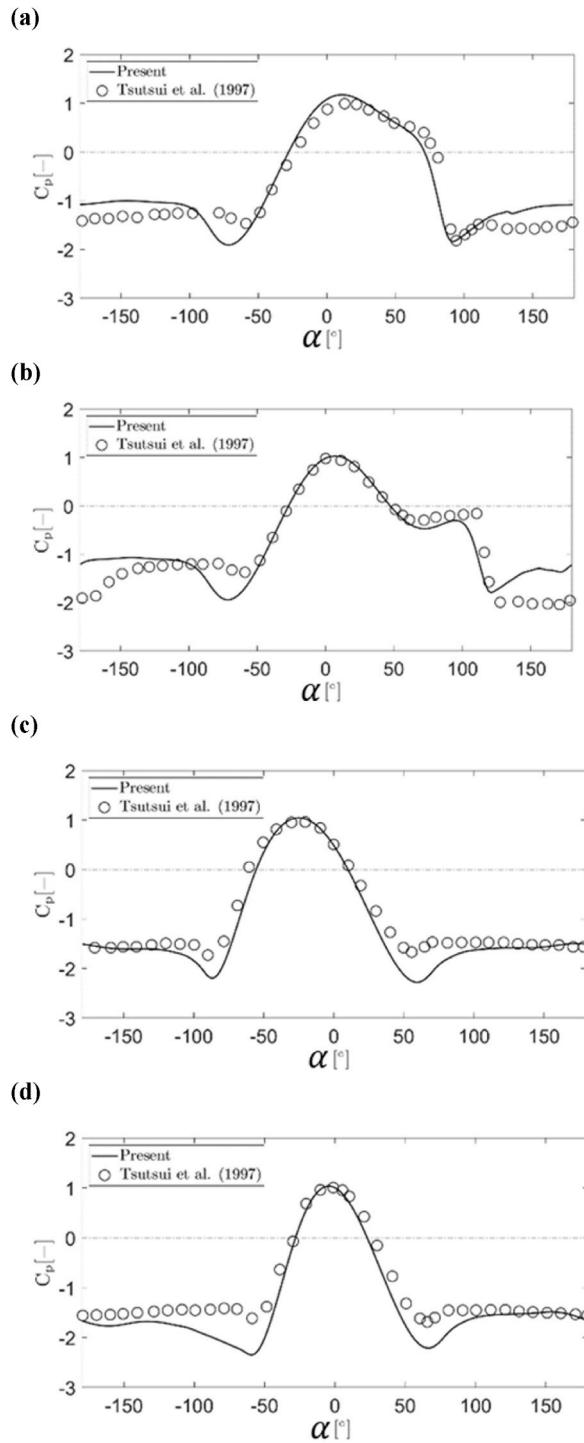

(b)

(c)

(d)

Fig. 7. Comparison between experimental measurements and present predictions of the pressure coefficient distribution on the surface of the large cylinder in (a) $\alpha = 90°$ and (b) $\alpha = 120°$ configuration; on the surface of the small cylinder in (c) $\alpha = 90°$ and (d) $\alpha = 120°$ configuration.

3.2.3. The application of hydrodynamic forces on piggyback pipeline

In the pipelaying model, the current directions are defined with respect to the vessel heading (pipelaying direction) shown in Fig. 8. Considering a fixed vessel heading, the incoming current $\overrightarrow{U}$ with $\theta = 0°$ represents a current direction that is in line with the vessel heading. θ is the angle between the current direction and the vessel heading.

It is proven numerically and experimentally that, at sufficiently high Re, flow past a cylinder will generate periodic force
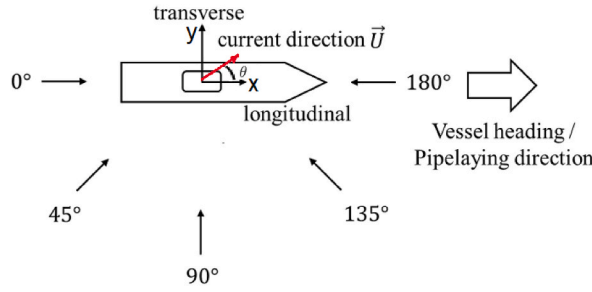
Fig. 8. The current direction with respect to the orientations of the pipelaying vessel in the global coordinate system.

components in the x- and y-directions, as shown in Fig. 4, due to vortex-shedding. The time varying force coefficients are difficult to be incorporated into the hydrodynamic model for pipelaying simulations. In the present study, mean force coefficients are used to calculate the hydrodynamic forces and these coefficients are obtained by non-dimensionalizing the time-averaged drag ($f_{x,m}$) and lift ($f_{y,m}$) forces per unit length calculated using the CFD simulations,

$$\overline{C}_{d,m} = \frac{f_{x,m}}{\frac{1}{2}\left|\vec{U}_{\text{inflow},m}\right|^2 \rho D_m} \tag{17}$$

$$\overline{C}_{l,m} = \frac{f_{y,m}}{\frac{1}{2}\left|\vec{U}_{\text{inflow},m}\right|^2 \rho D_m} \tag{18}$$

where $\vec{U}_{\text{inflow},m}$ is the inflow velocity perpendicular to the large cylinder's longitudinal axis; D_m is the diameter of the small and large cylinders where $m = 1$ for the large cylinder and $m = 2$ for the small cylinder. It should be noted that time-averaged forces are total forces that comprise form drag and skin friction.

A database of hydrodynamic coefficients is generated using CFD for both the pipeline and the piggyback cable with different combinations of Re and the flow angle α. In the present study, the hydrodynamic forces on a unit length of the pipeline are calculated based on the cross-flow principle [20]. For single pipelines, the drag forces are calculated by OrcaFlex directly based on the Re at the pipeline segments. However, for piggyback pipelines, the hydrodynamic coefficients are functions of both Re and the flow angle α, which could not be directly calculated using existing features of OrcaFlex. A user-defined module is therefore implemented through an external Python function that calculates the hydrodynamic forces and passes the force values to OrcaFlex. Local coordinate (x', y', z') with respect to the global coordinate (x, y, z) is shown in Fig. 9 for a pipeline segment. The local x' axis is in the direction from the
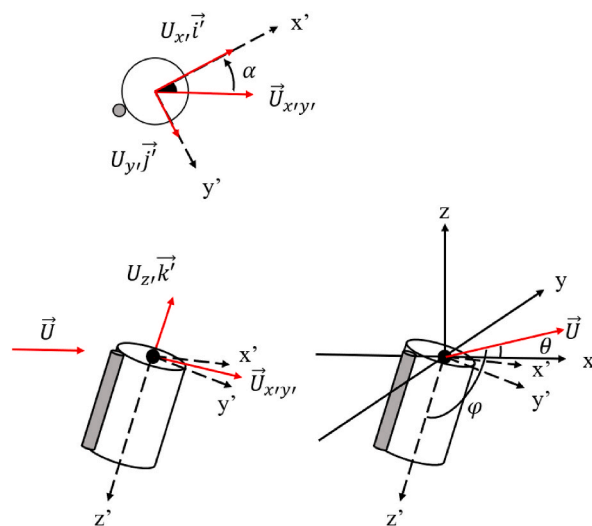

Fig. 9. Global and local coordinate system and the components of current velocity $\vec{U}$ in the local x', y' and z' axes of the pipe segment. θ is the current direction in the global coordinate system; φ is the angle between the current velocity $\vec{U}$ and local z' axis; α is the angle between $\vec{U}_{x'y'}$ and local x' axis, which is the same as the flow angle defined in Fig. 4.

center of the cable to the center of the pipeline and the local z' axis is along the longitudinal axis of the pipeline. θ is the current direction in the global coordinate system. φ is the angle between the current velocity $\vec{U}$ and local z' axis. $\vec{U}$ is first decomposed into the components at each pipeline segment with respect to its local axes ($\vec{U} = U_{x'}\vec{i} + U_{y'}\vec{j} + U_{z'}\vec{k}$) given by,

$$
\begin{bmatrix} U_{x'} \\ U_{y'} \\ U_{z'} \end{bmatrix} = U \begin{bmatrix} \vec{i} & \vec{j} & \vec{k} \end{bmatrix}^{\mathbf{T}} \begin{bmatrix} \cos\theta \\ \sin\theta \\ 0 \end{bmatrix}
$$

(19)

The fluid velocity normal to the pipeline, $\vec{U}_{x'y'} = U_{x'}\vec{i} + U_{y'}\vec{j} = \vec{U}_n$ is used to calculate the local Re values at the segment according to Equation (2). The flow angle at the pipeline cross section, α can be calculated using $U_{x'}\vec{i}$ and $\vec{U}_{x'y'}$ given by,

$$
\alpha = \cos^{-1}\left(\frac{U_{x'}}{\sqrt{U_{x'}^2 + U_{y'}^2}} \right)
$$

(20)

with α varying from 0° to 180°.

Finally, the database generated by the CFD simulations is used to interpolate the drag and lift coefficients using the calculated Re and α. Using this method, the hydrodynamic loads applied on each segment of the pipeline and the piggyback cable are dependent on θ, φ, α and the local Re as shown in Fig. 9. The detailed workflow of the user-defined procedure is shown in Fig. 10.

The simulations of the piggyback pipeline's response in the present study are based on the common engineering approach, i.e., the friction force along the local longitudinal cylinder axis is not considered. The same approach was used in other commercial engineering software, such as SIMLA [21].

3.3. Structural model

In the present study, a simulation model is constructed using OrcaFlex for the J-lay configuration with a water depth of 3000 m, as shown in Fig. 11. Stiffness and damping between nodes are modelled in three DOFs as spring-damper couples: (1) axial – the translational DOF between two nodes, (2) bending – the rotational DOF between the nodes' axial direction and (3) torsion – the rotational DOF in the segment's axial direction as shown in Fig. 12. For a pipeline segment subjected to internal and external pressures, the tension in the axial spring-damper couple is given by,

$$
T_e = EA\varepsilon + (1 - 2\nu) \bullet (p_0 a_0 - p_i a_i) + EA\lambda \frac{dl}{dt}\frac{1}{l_0} + k_{tt}\frac{\tau}{l_0}
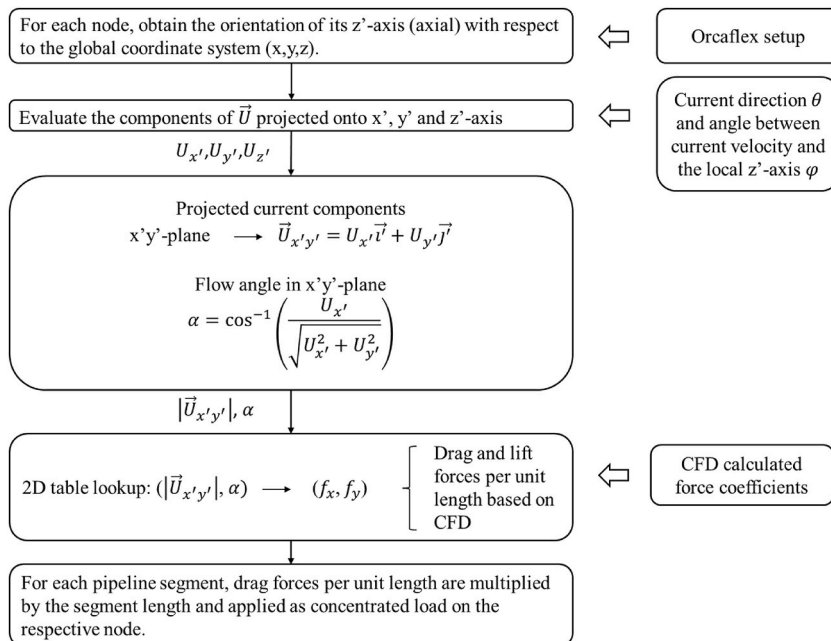$$

(21)

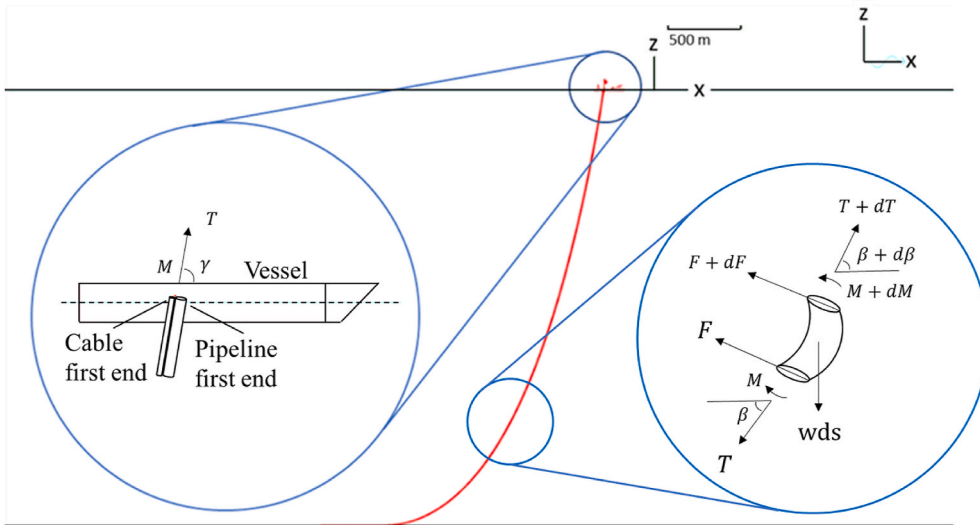**Fig. 10.** External force function implementation workflow.

Fig. 11. Orcaflex model of a pipelaying operation.
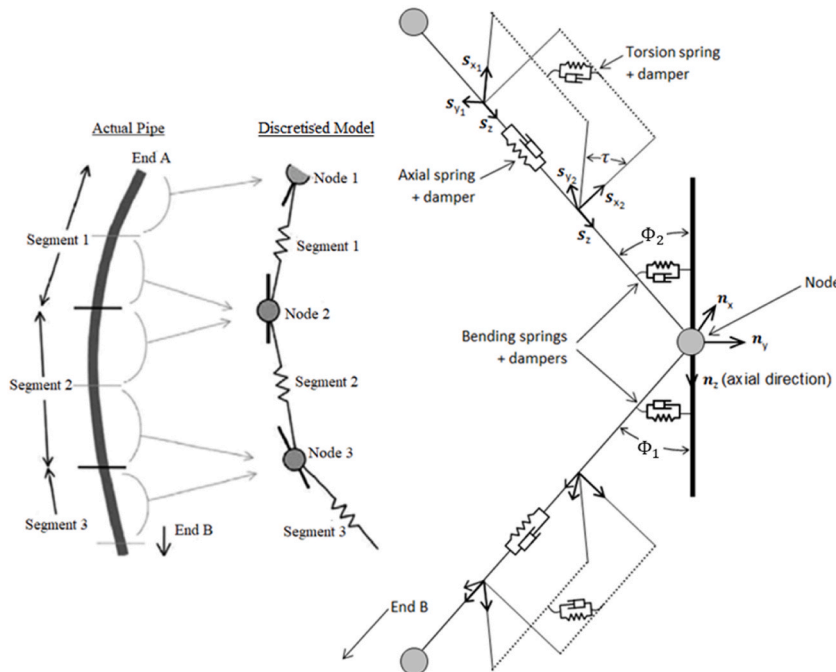

Fig. 12. Stiffness and damping model between nodes in Orcaflex [12].

where EA is the pipeline axial stiffness; ε represents the mean axial strain at the pipe wall; p_0 and p_i are the external and internal pressure forces, respectively; a_0 and a_i are the external and internal cross-sectional areas, respectively; ν is the Poisson's ratio; l is the instantaneous segment length at time t; l_0 is the unstretched segment length; and λ is the physical axial damping coefficient ($\lambda = 0$ for static analysis). The term k_{tt} represents a direct stiffness coupling between tension and torque when the pipeline torsion is accounted for with τ representing the pipeline twist angle.

Fig. 12 shows the stiffness and damping models between nodes. A node connecting two segments has a bending spring-damper on each side. The degree of bending on each side is quantified by the relative bend angle, Φ between the node's axial direction and the segment's axial direction (shown in Fig. 12). The curvature c can then be calculated using $c = \alpha/(0.5l_0)$, and the bending moment due to the curvature on one side of the node is given by

$$M = EIc + \lambda_b \frac{dc}{dt} \tag{22}$$

where EI is the bending stiffness and λ_b is the physical damping coefficient for bending ($\lambda_b = 0$ for static analysis). The total bending moment on the node can thus be calculated by the summation of bending moments experienced on both sides.

With the bending moment being defined on nodes, each line segment connecting two nodes is modelled as a stiff rod (i.e., with negligible bending) in which the bending moment varies linearly along the segment. The shear force along the segment can then be represented by the rate of change of bending moment along its length given by,

$$F_s = \frac{M_2 - M_1}{l} \tag{23}$$

where M_2 and M_1 are the bending moments at either end of the segment and l the instantaneous segment length. The shear force is acting in the cross-section of the pipeline.

Finally, the torsion along a segment is characterized by the twist angle τ, defined as the change in axial rotation for two adjacent nodes resolved in the bending plane given by,

$$T = k\frac{\tau}{l_0} + k_{tt}\varepsilon + \lambda_c\frac{d\tau}{dt} \tag{24}$$

where k is the torsional stiffness and λ_c is the physical damping coefficient for torsion ($\lambda_c = 0$ for static analysis). Based on the line model described above, the static and dynamic loads on the catenary can be obtained by solving the force and moment equilibrium along the entire pipeline efficiently.

The pipeline and the piggyback cable in the proposed method are modelled as two separate lines with element sizes of 2.5 m and 1.25 m, respectively. In order to simulate the condition in which both lines are held together via straps in a piggyback pipeline bundle, two contact relationships have been defined in a piggyback pipeline model. For the first contact relationship, the straps are placed along the pipeline with a 2.5 m spacing to restrict the motions of the cable. The cable is modelled as a smooth spline curve. Therefore, the contact loads are transferred between the finite element nodes at the pipeline and the piggyback cable. The second contact relationship prevents the segment of the pipeline and the cable between the straps from penetrating into each other when they are in contact. A graphical illustration of contact models is shown in Fig. 13. The reaction force at each contact is treated as elastic and can be calculated by,
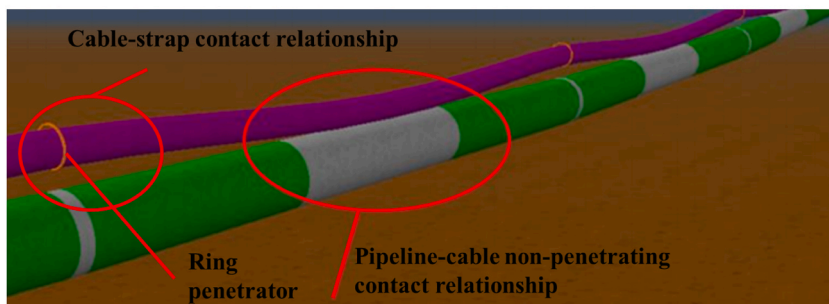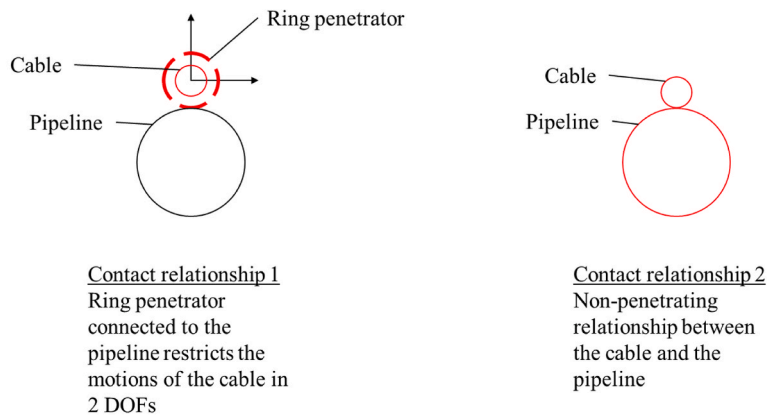

Fig. 13. Graphical illustration of line contact modelling in OrcaFlex. Reproduced from Ref. [22].
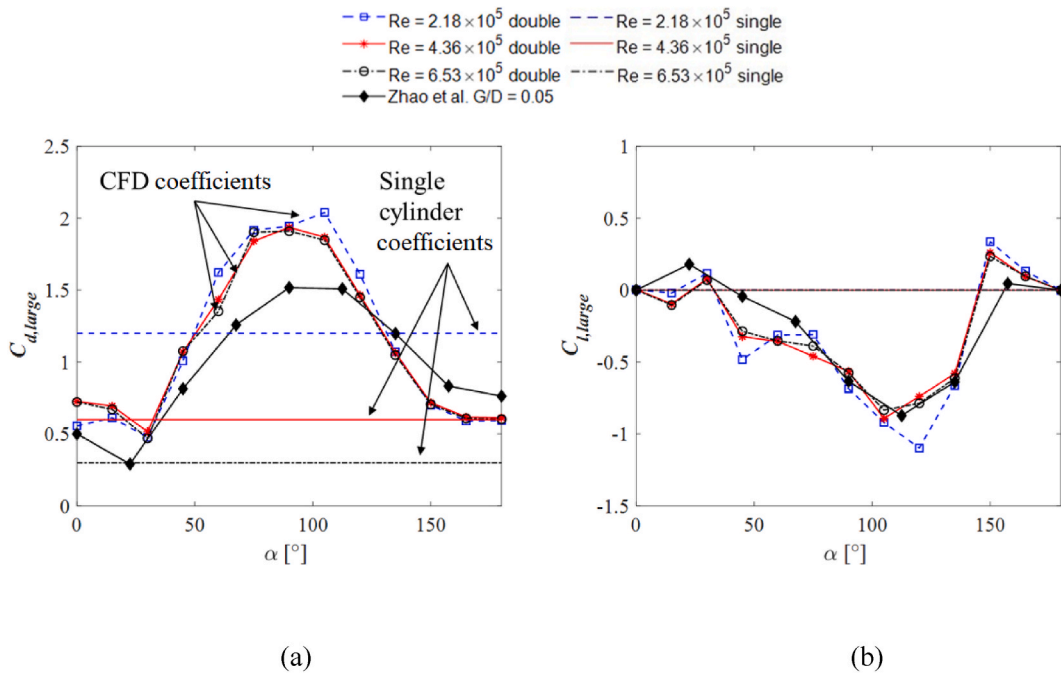
Fig. 14. Variation of mean force coefficients on the large cylinder with α. (a) C_d of large cylinder, (b) C_l of large cylinder. For comparison, the force coefficients of a smooth single cylinder corresponding to the respective Re are plotted in the same figure.

Fig. 15. Variation of mean force coefficients on the small cylinder with α. (a) C_d of small cylinder, (b) C_l of small cylinder. For comparison, the force coefficients of a smooth single cylinder corresponding to the respective Re are plotted in the same figure. For single cylinder the drag coefficients are about 1.2.
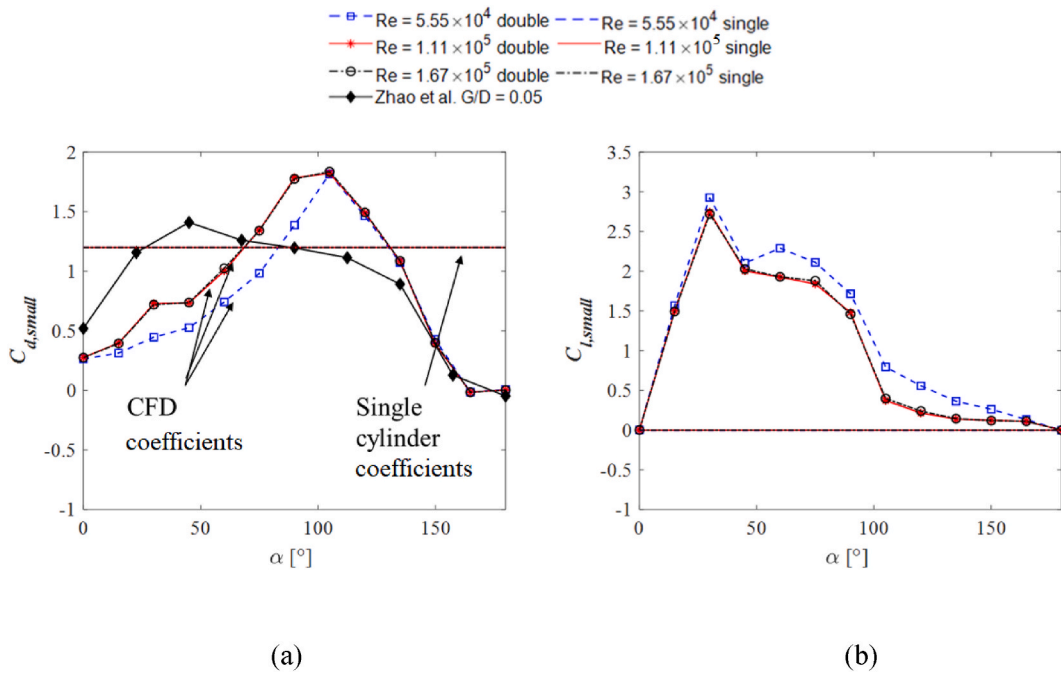
$$f_R = r(p)a \tag{25}$$

where r is the reaction force per unit contact area and it is a function of the penetration depth p while a is the contact area per unit length.

The pipelaying vessel is represented as a rigid body fixed to the global reference frame in the model. The first end (vessel end) of the pipeline is assumed to have infinite connection stiffness to simulate the HOC boundary conditions. A constant departure angle of 80° is assumed for simulations. The second end of the pipeline is located at approximately 430 m from TDP and is anchored to the seabed with infinite connection stiffness simulating the boundary conditions of the installed section of the pipeline. The seabed is modelled as an elastic support with the normal reaction force proportional to the penetration depth of the pipeline. The initial as-laid route is simplified as a straight-line section supported by the seabed. Another simplification is that the wave loads are not included in the present study but can be easily enabled in the simulation model. The reason for excluding the wave loads is to facilitate the benchmarking of the investigated model.
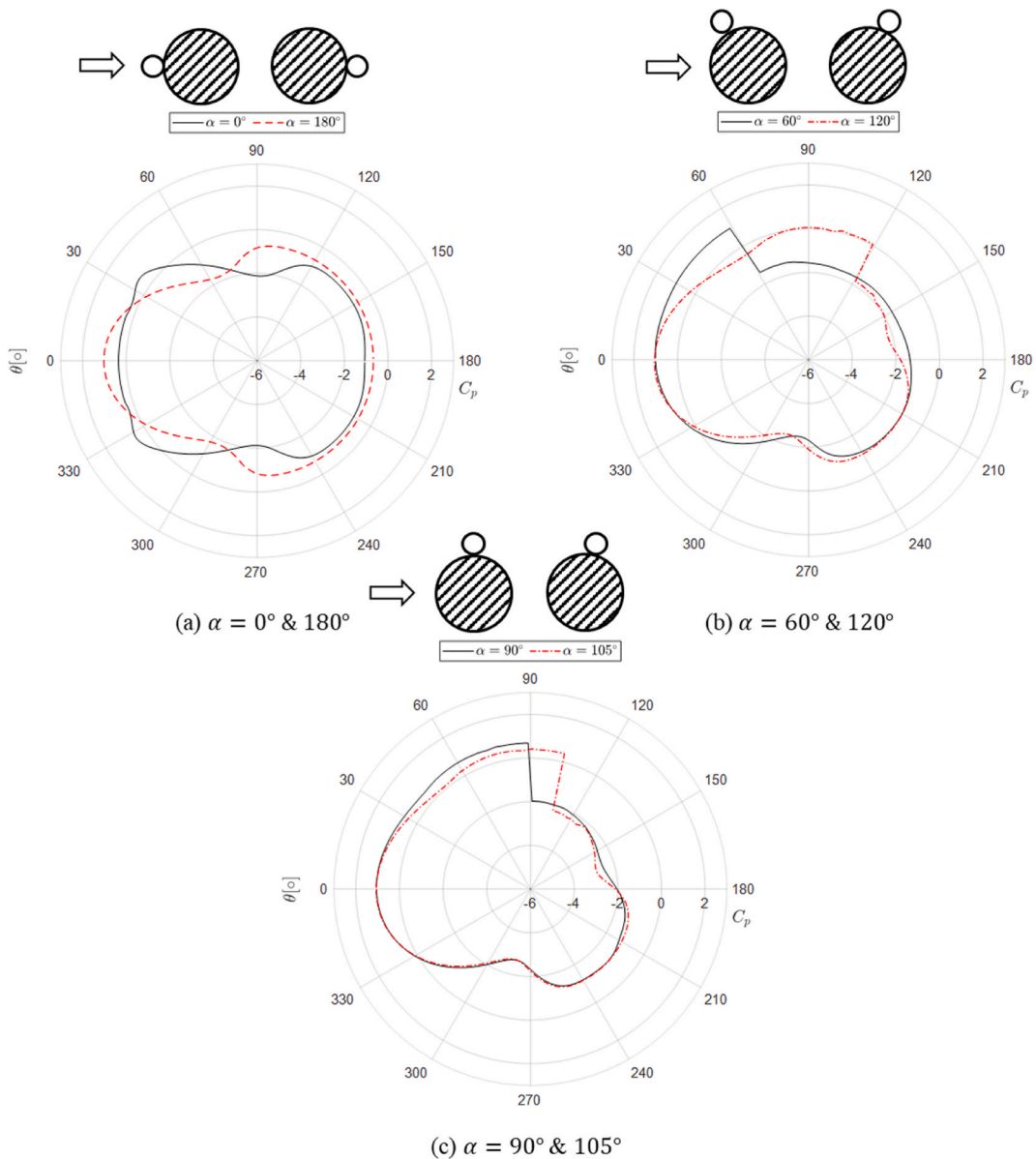

(a) $\alpha = 0°$ & 180°

(b) $\alpha = 60°$ & 120°

(c) $\alpha = 90°$ & 105°

Fig. 16. Mean pressure coefficient, $\overline{C}_p$ contours on the large cylinder in different orientations for $Re = 6.53 \times 10^5$.

4. Results and discussions for CFD simulations

The variation of time-averaged drag coefficients ($\overline{C}_d$) and lift coefficients ($\overline{C}_l$) for both large and small cylinders in the piggyback configuration in different flow directions are shown in Figs. 14 and 15. Commonly adopted values of $\overline{C}_d$ and $\overline{C}_l$ for a smooth single cylinder [23] at the corresponding Re numbers are plotted in comparison for easier interpretation of the CFD results. As shown in Figs. 14a and Fig. 15a, the $\overline{C}_d$ values in a piggyback configuration are highly sensitive to the change in the flow direction (α). The largest $\overline{C}_d$ value is observed for α in a range of approximately $75° < \alpha < 105°$ and the lowest $\overline{C}_d$ value is observed when $\alpha \approx 0°$ and $\alpha \approx 180°$. When $75° < \alpha < 105°$, depending on the Re, the $\overline{C}_d$ values can be underestimated by approximately 1.5–6 times when the $\overline{C}_d$ values of single cylinders are used instead of the CFD-computed coefficients for piggyback configuration. As shown in Fig. 14a, the $\overline{C}_d$ values in a piggyback configuration are not sensitive to the change in Re. For the three investigated Re, the CFD-calculated $\overline{C}_d$ curves are very close to each other except when α is closer to $0°$. It is also observed that at $\alpha = 0°$ and $180°$, $\overline{C}_d$ increases as Re increases. However, at $\alpha = 90°$, $\overline{C}_d$ decreases as Re increases. This highlights some inconsistencies with regards to the behaviour of hydrodynamic loads in relation to Re at the different flow angles.
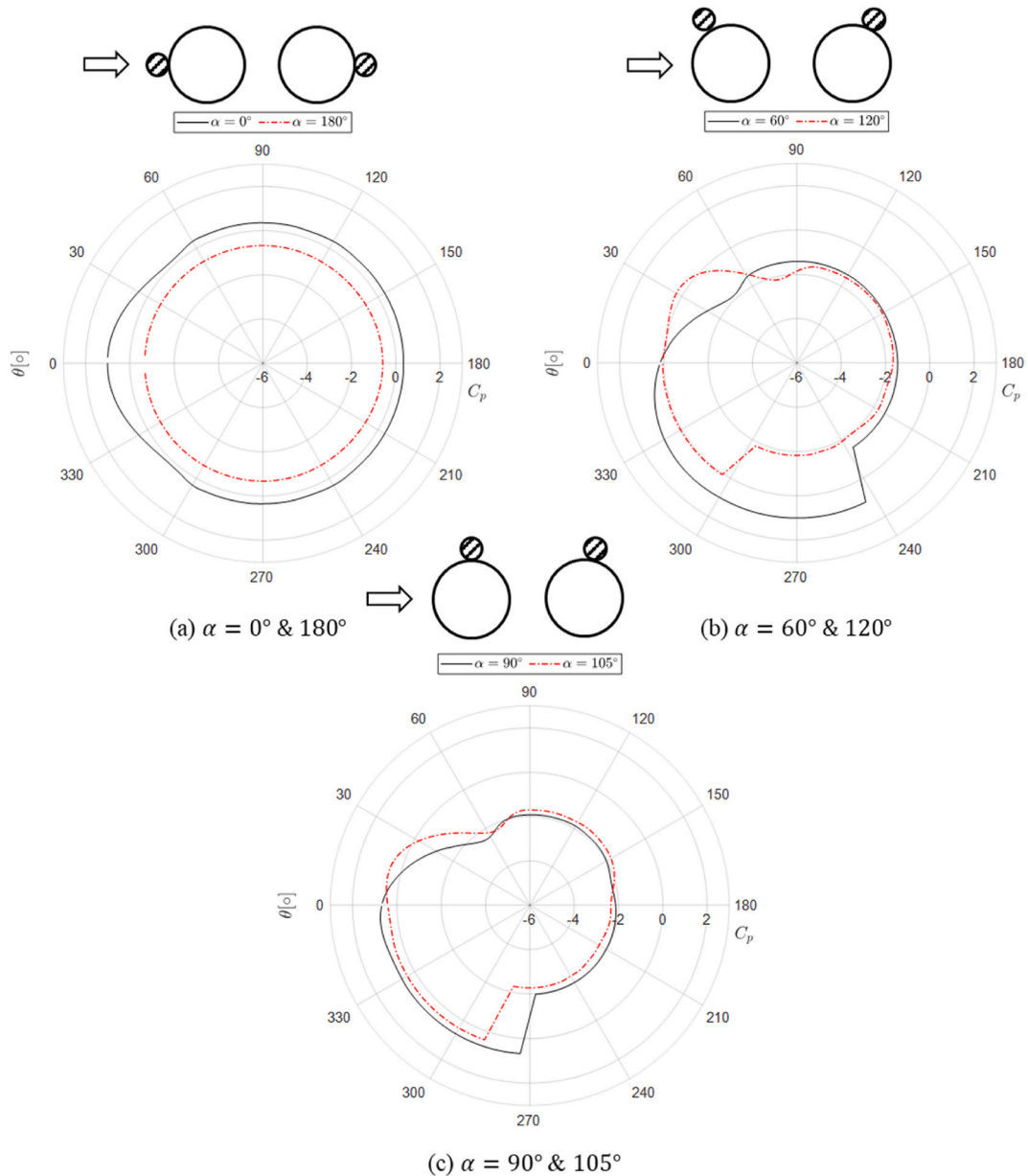

Fig. 17. Mean pressure coefficient, $\overline{C}_p$ contours on the small cylinder in different orientations for $Re = 1.67 \times 10^5$.

The influence of the small cylinder on the large cylinder can be better understood by visualizing the pressure distributions on the cylinder surfaces for different analysed flow directions. In the case of external flow around bluff bodies such as investigated cylinder bundles, the viscous component of total drag force is negligible and the main contribution comes from the pressure drag, also known as the form drag. Achenbach [24] investigated the cross-flow pressure and skin friction around a circular cylinder in flow up to $Re = 5\times 10^6$ and discovered that the contribution of skin friction to the total drag is relatively unimportant. Pressure drag is computed as the integral of the streamwise direction (x-axis) component of the pressure around the cross section of the cylinder; therefore, the pressure distribution governs the magnitude of the drag force on the cylinders bundle. Time-averaged pressure coefficient ($\overline{C}_p$) distributions for selected cases are shown in Fig. 16 for the large cylinder and in Fig. 17 for the small cylinder. The pressure coefficient is defined as,

$$\overline{C}_p = \frac{p - p_\infty}{\frac{1}{2}\left|\overrightarrow{U}_{\text{inflow}}\right|^2 \rho} \tag{26}$$

where p is the flow pressure on the respective cylinder and p_∞ is the free stream flow pressure. From Fig. 16a, it is apparent that when the small cylinder is placed upstream ($\alpha = 0°$) of the large cylinder, the pressure in the area close to the stagnation point is reduced as the shape in this configuration is more streamlined than the single cylinder. When the small cylinder is placed in the wake of the large cylinder ($\alpha = 180°$), it decreases the suction at the back side of the large cylinder. At higher Re, both configurations ($\alpha = 0°, \alpha = 180°$) experience higher pressure drag than that of an isolated cylinder, as illustrated in Fig. 14a and Fig. 16a. When the small cylinder is placed in configurations other than $\alpha = 0°$ and $\alpha = 180°$, the $\overline{C}_p$ distribution on the large cylinder becomes significantly asymmetric with respect to the streamwise direction. Two effects can be observed when the small cylinder is moved from $\alpha = 0°$ towards $\alpha = 90°$ position (Fig. 16b, c, Fig. 17b–c) namely, an increase in the pressure on the front face of the cylinders bundle, especially close to the point where the cylinders are attached. An increase in the suction at the back side of the cylinders bundle is also observed. As expected, these effects become the strongest when the piggyback position is close to $\alpha = 90°$. The asymmetric $\overline{C}_p$ distribution also results in a non-zero time-averaged lift force. As shown in Fig. 14b, the $\overline{C}_l$ values on the large cylinder peak when the small cylinder is positioned at $105° < \alpha < 120°$ depending on the Re number.

The largest $\overline{C}_d$ value of the small cylinder is observed when it is positioned at $\alpha = 105°$ as it results in the highest pressure difference in the streamwise direction, as illustrated by the $\overline{C}_p$ contour in Fig. 17c. The largest $\overline{C}_l$ value of the small cylinder occurs when it is positioned at $\alpha = 30°$.

A further insight on the flow behavior can be gained by analyzing the distribution of the instantaneous spanwise vorticity field around the cylinders bundle presented in Figs. 18 and 19. The effect of the piggyback configuration is primarily visible in the
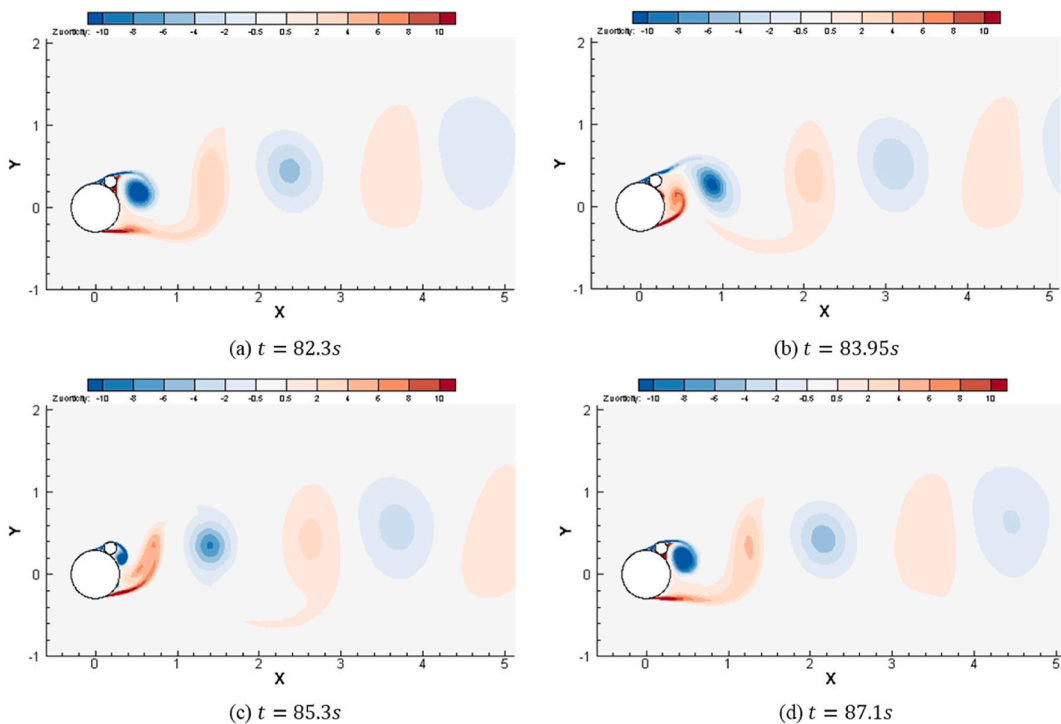

(a) $t = 82.3s$

(b) $t = 83.95s$

(c) $t = 85.3s$

(d) $t = 87.1s$

Fig. 18. The development of vortex shedding shown by instantaneous vorticity contours behind two smooth cylinders orientated in $\alpha = 120°$ for $Re = 2.18 \times 10^5$ evaluated at the large cylinder. Time steps from $82.3s$ to $87.1s$ are shown. Contour levels from $-10s^{-1}$ to $10s^{-1}$ are plotted.
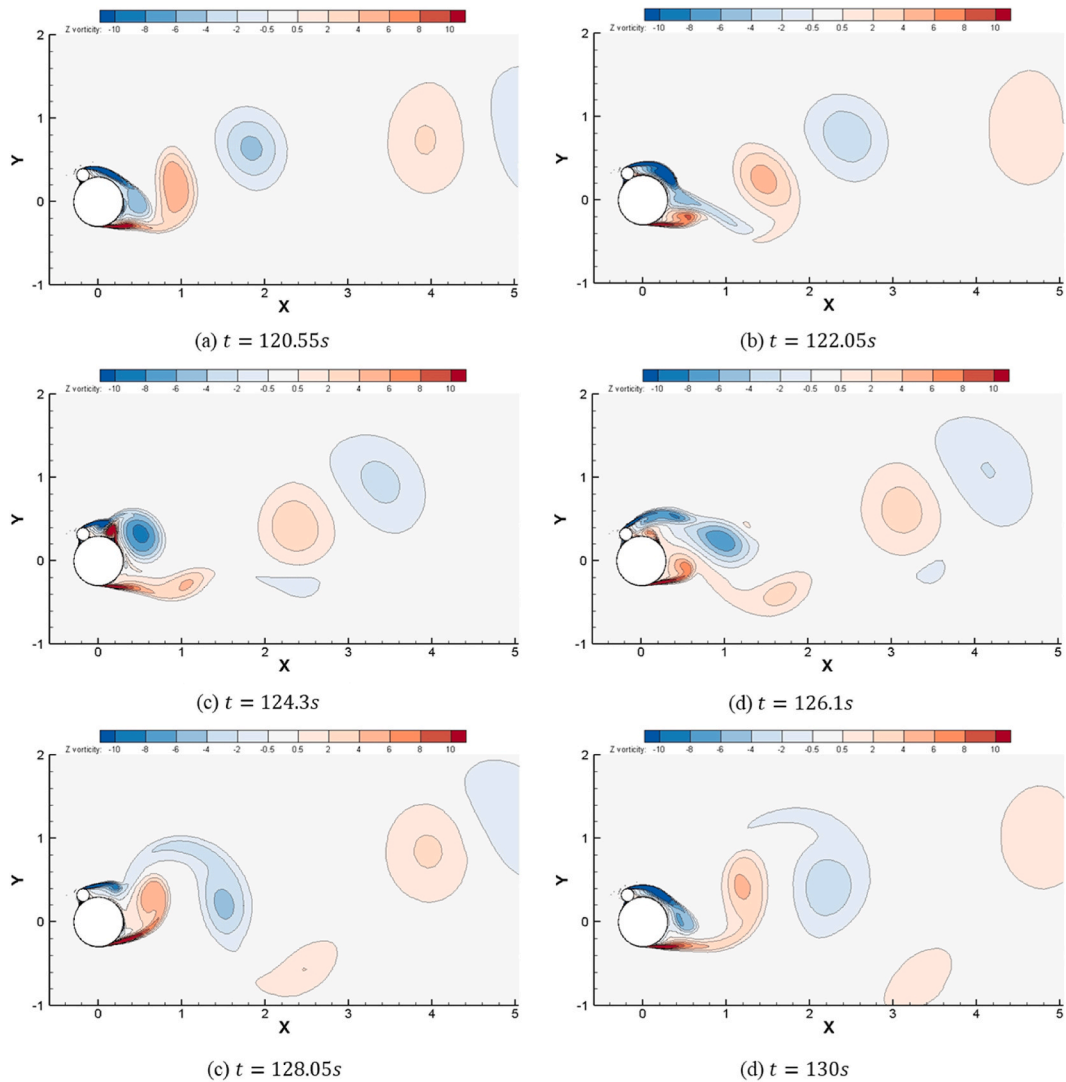
Fig. 19. The development of vortex shedding shown by instantaneous vorticity contours behind two smooth cylinders arranged at $\alpha = 60°$ for $Re = 2.18 \times 10^5$ evaluated at the large cylinder. Time steps from $120.55s$ to $130s$ are shown. Contour levels from $-10s^{-1}$ to $10s^{-1}$ are plotted.

breakdown of the symmetry in the wake. Large recirculation regions are formed behind the attachment point of the two cylinders (see Fig. 18 and Fig. 19c) which is the reason for the increased suction at the back side of the cylinders bundle.

5. Pipelaying analysis

5.1. Analysis setup

The selected piggyback configuration consists of a 20″ pipeline (0.508 m) and a DEH cable with a diameter of 0.150 m. For the pipeline, its wall thickness satisfies the minimum requirement to avoid local buckling according to DNV-ST-F101 [13], as described by Herdiyanti [25]. The DEH cable contains a copper wire core with an outer layer of High-Density Polyethylene (HDPE). Its equivalent structural properties are derived from the structural properties of the HDPE and the copper wire core.

For the equivalent line method, the equivalent pipeline (pipeline and DEH cable) would have the structural properties (axial, bending and torsional stiffnesses) of the pipeline and the submerged weight of the pipeline and the DEH cable. The hydrodynamic loads of the equivalent line are calculated based on its equivalent diameter as shown in Fig. 3. The properties of the pipeline, the DEH cable and the equivalent line are shown in Table 1.

Table 1
Geometry data and mechanical properties of pipeline and piggyback cable.

	20″ pipe	cable	Equivalent piggyback pipeline
Pipe outer diameter [m]	0.508	0.150	0.738
Coating thickness [m]	0.04	–	–
Pipe inner diameter [m]	0.441	–	0.441
Bending stiffness [kN·m^2]	2.91×10^5	72.10	2.91×10^5
Axial stiffness [kN]	1.03×10^7	2.49×10^5	1.03×10^7
Torsional stiffness [kN·m^2/rad]	2.24×10^5	55.46	2.24×10^5
Young's modulus [GPa]	206	1.5	206
Weight in air [kN/m]	4.371	0.318	4.689
Weight in water [kN/m]	1.642	0.140	1.781

5.2. Overview of models

In the present study, three models are investigated:

- Equivalent diameter method with classical hydrodynamic coefficients
- Two-line method with classical hydrodynamic coefficients
- CFD two-line method with CFD hydrodynamic coefficients

A detailed description of the three models is given in Table 2. The classical hydrodynamic coefficients used in the equivalent diameter and the two-line method refer to smooth cylinder drag coefficients $\overline{C}_d$ that are based on the experimental results obtained by Achenbach [24] and Heinecke [25]. Due to axial symmetry, the $\overline{C}_d$ values only depend on Re number. The lift coefficients $\overline{C}_l$ used in the equivalent line model and the two-line method are taken as zero. The $\overline{C}_d$ and $\overline{C}_l$ values used in the CFD two-line method for the different flow velocities and directions are obtained through linear interpolation based on the results plotted in Figs. 14 and 15.

5.3. Load cases

The nature of ocean currents is dynamic. However, assuming that the current velocity is slowly varying locally, submerged pipelines can be considered as exposed to steady current flow, which varies only with the water depth. In the present study, constant current environment is assumed and mean (time-averaged) hydrodynamic forces on pipeline segments are considered in simulation. The current velocity is 1.5 m/s at the sea surface, and it reduces to 0.075 m/s at the seabed, as shown in Fig. 20. Thirteen load cases with different global current directions ($\theta = 0°, 15°, \ldots, 180°$) are simulated. The case with $\theta = 0°$ represents current in the pipelaying direction (following sea), while the case with $\theta = 180°$ represents an opposing current with respect to the pipelaying direction (head sea).

Table 2
Summary of modelling methods used in the present study.

| Method	Equivalent diameter method	Two-line method	CFD Two-line method
Description	Equivalent diameter method with classical hydrodynamic coefficients	Two-line method with classical hydrodynamic coefficients	Two-line method with CFD hydrodynamic coefficients
Number of lines modelled	1	2	2
Contact between pipeline and piggyback	No	Yes	Yes
Drag coefficient	- Smooth cylinder, Re number dependent drag coefficients are used. - Total drag force evaluated at one cylinder.	- Smooth cylinder, Re number dependent drag coefficients are used. - The drag force is calculated separately at each cylinder. The total drag force is taken as the summation of the forces on the pipeline and cable.	- Drag and lift coefficients for pipeline and cable are evaluated separately using CFD for 3 different levels of flow velocity and 13 incoming flow directions [0° 180°] - Coefficients for intermediate current velocities and angles are linearly interpolated. - Drag and lift forces are calculated separately at each cylinder. Total drag and lift forces are taken as the summation of the forces on the pipeline and cable.
Lift coefficient	0	0	- Lift coefficients are obtained as per the method outlined for drag coefficients
Comments	No interaction between pipeline and piggyback for both hydrodynamic and structural model	No interaction between pipeline and piggyback for hydrodynamic model	Interaction between pipeline and piggyback for both hydrodynamic and structural model
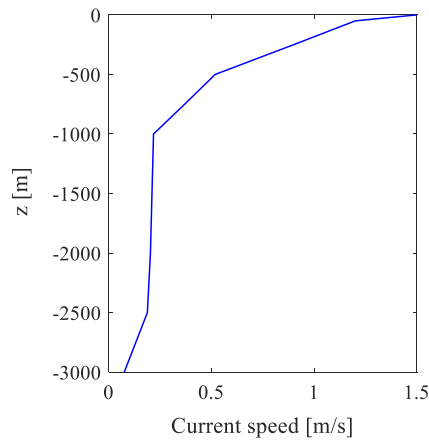
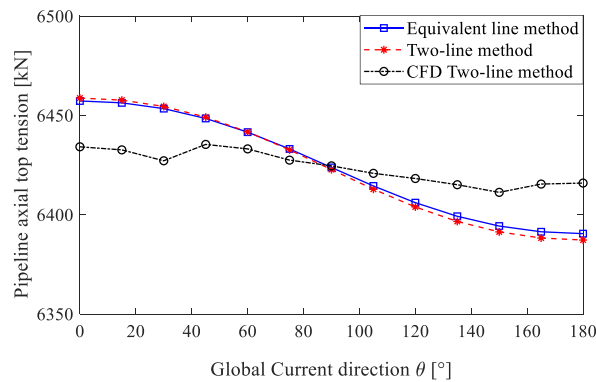**Fig. 20.** Current velocity profile.

Fig. 21. Pipeline axial top tension for a 20″ piggyback pipeline in different global current directions.

5.4. Results of pipelaying simulations

5.4.1. Pipeline axial top tension

The axial tensions at the top of the pipeline plotted against the current direction are shown in Fig. 21. All models predict a similar trend of the pipeline top tension in which the tension is highest when the current direction and the pipelaying direction coincide ($\theta = 0°$). The tension reduces as the current direction increases, and when the current is opposing the pipelaying direction ($\theta = 180°$), the tension is at its minimum. This is simply because the drag force acts in the direction that supports the suspended catenary weight.

The pipeline axial top tensions predicted by the equivalent diameter method and the two-line method are in close agreement as the top tension is mainly influenced by the submerged weight of the piggyback pipeline. The CFD two-line method estimates 0.4% lower
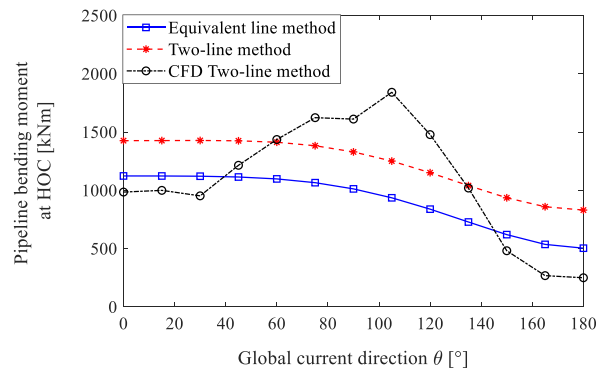

Fig. 22. Pipeline bending moment at HOC exit for a 20″ piggyback pipeline in different global current directions.

tension than the two-line method when the current is coming from $\theta = 0°$ and 0.4% higher tension than the two-line method when the current is coming from $\theta = 180°$. This is caused by the difference in the applied drag coefficients between the models. With reference to Fig. 14a, for $\theta = 0°$, the drag coefficient predicted by two-line method increases as Re reduces with the increasing depth. In contrast, for CFD two-line method, the drag coefficient reduces as Re reduces with the increasing depth.

5.4.2. Pipeline bending moment at HOC exit

The pipeline bending moment at HOC plotted against the current direction is shown in Fig. 22. The two-line method consistently predicts a higher bending moment at HOC as compared to the equivalent diameter method in all current directions. For the 20″ piggyback pipeline with the geometries presented in Table 1, the Re of the pipeline for the two-line model is about 20% smaller than that of the equivalent pipeline for the equivalent diameter model when the inflow current direction and velocity are the same. As shown in Fig. 14a, the mean drag coefficient of the large cylinder is dependent on the Re, and a smaller Re results in a higher $\overline{C}_d$. At the same time, the $\overline{C}_d$ value of the small cylinder is approximately 1.2 and independent of Re, as shown in Fig. 15a. The two effects result in higher $\overline{C}_d$ values for both the pipeline and the piggyback cable in comparison with the equivalent-diameter pipeline. Therefore, the total drag force in the two-line model is larger than the drag force acting on the equivalent-diamater pipeline.

Among the three models, the CFD two-line method gives the lowest HOC bending moment when the incoming current direction is relatively in-line with the pipelaying direction, i.e., when $\theta < 30°$ and $\theta > 150°$. When the current is coming from the transverse direction, i.e., $75° < \theta < 105°$, the CFD two-line method gives significantly higher bending moments at HOC than the other two simplified methods. It is observed that in the current angle $\theta = 105°$, the CFD two-line method predicts a bending moment at HOC that is approximately 47% higher than the result predicted by the two-line method. As shown in Figs. 14a, 15a and 16c and 17c, the CFD-calculated $\overline{C}_d$ values of both the pipeline and the piggyback cable are the highest when $= 105°$. When subjected to current loadings from this direction, the CFD two-line method predicts the highest transverse deflection, which results in the highest bending moments at the HOC. A comparison of transverse deflection along the pipeline predicted using three different modelling methods when the current is coming from $\theta = 105°$ is shown in Fig. 23. It is shown clearly in Fig. 23 that both the equivalent-diameter and two-line methods, which do not consider the hydrodynamic interactions between the pipeline and the piggyback cable, estimate smaller pipeline transverse deflections. It indicates that the CFD two-line method can take into account the more realistic hydrodynamic effect on a piggyback configuration that changes in accordance with the direction of the incoming current.

5.4.3. Pipeline maximum bending moment at sagbend

The pipeline maximum bending moments at sagbend plotted against the current direction are shown in Fig. 24. All three models predict low sagbend bending moment when $\theta = 0°$ and high sagbend bending moment when $\theta = 180°$. The pipeline maximum bending moment at sagbend predicted by the equivalent-diameter and two-line methods are in close agreement. The CFD two-line method estimates a 2% higher bending moment than the two-line method when $\theta = 0°$ and a 2% lower bending moment than the two-line method when $\theta = 180°$. This is due to the increase in drag coefficient predicted by the two-line method as Re reduces with the increasing depth.

6. Conclusions

The present study started by scrutinizing the possibility of considering the hydrodynamic and structural interactions between the pipeline and the piggyback cable in the piggyback pipelaying simulation. An improved method (CFD two-line method) for simulating piggyback pipelaying is proposed. The hydrodynamic interaction between the pipeline and the piggyback cable subjected to different current directions is modelled using CFD simulations. A user-defined external function is implemented in OrcaFlex to calculate the hydrodynamic forces on the piggyback pipeline. In the structural model, the pipeline and the piggyback cable are modelled separately with contacts between them. Two alternative methods, i.e., equivalent-diameter and two-line methods, have been investigated in the
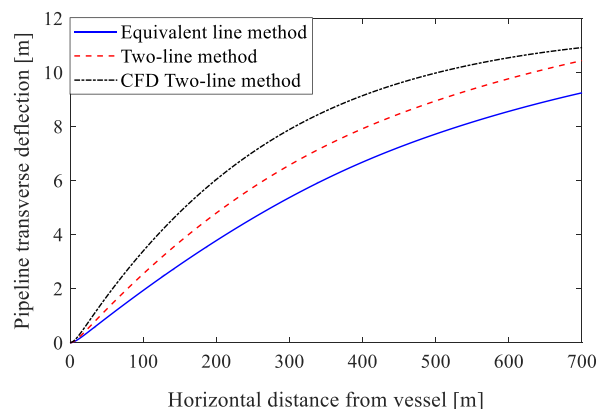

Fig. 23. Pipeline transverse deflection for a 20″ piggyback pipeline in $\alpha = 105°$ current calculated using different methods.
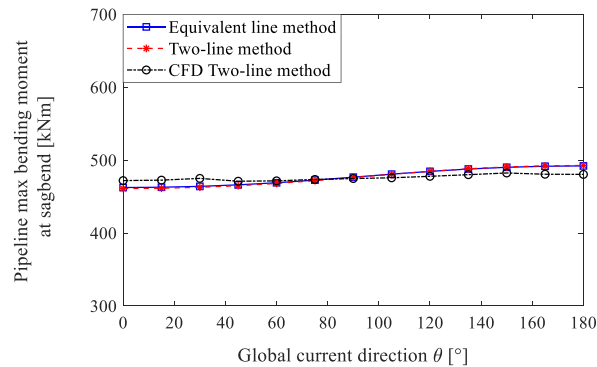
Fig. 24. Pipeline max bending moment at sagbend for a 20″ piggyback pipeline in different global current directions.

present study and the results are compared with the present CFD two-line method.

The results presented and discussed in the manuscript lead to the following remarks:

- CFD simulations show that the flow behaviour undergoes drastic changes when the single cylinder configuration is replaced with the piggyback pipeline configuration, i.e. two cylinders are attached to each other without gap. The variation of time-averaged drag coefficients ($\overline{C}_d$) and lift coefficients ($\overline{C}_l$) for both large and small cylinders in the piggyback configuration are highly sensitive to the change in the flow direction (α). The largest $\overline{C}_d$ value is observed for α in a range of approximately $75° < \alpha < 105°$.
- The equivalent diameter method is in good agreement with the two-line method in predicting the top tension and maximum sagbend bending moment of the pipeline. In general, the two-line method predicts higher HOC bending moments than the equivalent diameter method due to a higher hydrodynamic load prediction.
- The equivalent diameter method is found to be not conservative for the piggyback pipelaying analysis when the current comes from the side as compared to the CFD two-line method. The maximum bending moment at HOC is significantly increased for the CFD two-line method because the interaction between the pipeline and the piggyback cable results in not only a higher mean drag coefficient $\overline{C}_d$ but also the combination of drag and lift forces for the transverse currents. Extreme care should be taken when calculating the maximum bending load of the piggyback pipeline subjected to the transverse current.
- In order to reduce the cross-flow drag and lift forces on the piggyback pipeline, it is preferred to lay the pipelines at $0°$ or $180°$ with respect to the incoming current. When the transverse current could not be avoided during the laying operation, the top tension can be increased to reduce the transverse deflection of the piggyback pipeline.
- The bending moment at HOC is the most critical parameter for the piggyback pipelaying operation and should be used to define the allowable operation condition.

Declaration of competing interest

The authors declare that they have no known competing financial interests or personal relationships that could have appeared to influence the work reported in this paper.

Data availability

No data was used for the research described in the article.

References

[1] Nysveen A, Kulbotten H, Lervik JK, Børnes AH, Høyer-Hansen M, Bremnes JJ. Direct electrical heating of subsea pipelines – technology development and operating experience. IEEE Trans Ind Appl 2007;43(1).
[2] Heggdal OA. Strapping machine (U.S. Patent No. 8858121 B2). U.S. Patent and Trademark Office; 2014.
[3] Lenci S, Callegari M. Simple analytical models for the J-lay problem. Acta Mech 2005;178:23–39.
[4] Jensen GA, Säfström N, Nguyen TD, Fossen TI. A nonlinear PDE formulation for offshore vessel pipeline installation. Ocean Eng 2010;37(4):365–77.
[5] Gong S, Xu P, Bao S, Zhong W, He N, Yan H. Numerical modelling on dynamic behaviour of deepwater S-lay pipeline. Ocean Eng 2014;88:393–408.
[6] Brany AM. Per. Damsleth and C. Gil, "Effect of pipeline thermal expansion on direct electric heating cable. In: Proceedings of the ASME 2013 32nd international conference on ocean, offshore and arctic engineering. France: Nantes; 2013.
[7] Kamarudin MH, Thiagarajan KP, Czajko A. Analysis of current-induced forces on offshore pipeline bundles. Melbourne, Australia: 5th International Conference on CFD in the Process Industries; 2006.
[8] Branković M, Zeitoun H, Sutherland J, Pearce A, Jacobsen V, Sabavala H, Tørnes K, Cumming G, Willcocks J. Physical modelling of hydrodynamic loads on piggyback pipelines in combined wave and current conditions. In: Proceedings of the ASME 2010 29th international conference on ocean. Shanghai, China: Offshore and Arctic Engineering; 2010.
[9] Janocha MJ, Ong MC. Vortex-induced vibrations of piggyback pipelines near the horizontal plane wall in the upper transition regime. Mar Struct 2021;75: 102872.

[10] Jakobsen ML, Sayer P. Hydrodynamic forces on piggyback pipelines. In: Proceedings of the 5th international offshore and polar engineering conference; 1995. The Hague, The Netherlands.

[11] Weller H, Tabor G, Jasak H, Fureby C. A tensorial approach to computational continuum mechanics using object-oriented techniques. Comput Phys 1998;12 (issue 6).

[12] Orcina. OrcaFlex user manual. UK: Cumbria; 2011., Version 9.4a.

[13] Det Norske Veritas AS. DNVGL-ST-F101 Submarine pipeline systems. Oslo, Norway: OFFSHORE STANDARD; 2017.

[14] Rosetti GF, Vaz G, Fujarra ALC. URANS calculations for smooth circular cylinder flow in a wide range of Reynolds numbers: solution verification and validation. J Fluid Eng 2012;134(12):121103.

[15] Menter FR, Kuntz M, Langtry R. Ten years of industrial experience with the SST turbulence model. In: Proceedings of the fourth international symposium on turbulence, heat and mass transfer. Turkey: Antalya; 2003. p. 625–32.

[16] Menter FR. Two-equation eddy-viscosity transport turbulence model for engineering applications. AIAA J 1994;32(8):1598–605.

[17] Palkin E, Mullyadzhanov R, Hadziabdic M, Hanjalic K. Rotary oscillations control of flow around cylinder at Re = 1.4 × 105. AIP Conf Proc 2016;1770:030075.

[18] Tsutsui T, Igarashi T, Kamemoto K. Interactive flow around two circular cylinders of different diameters at close proximity. Experiment and numerical analysis by vortex method. J Wind Eng Ind Aerod 1997;69:279–91. –71.

[19] Zhao M, Cheng L, Teng B, Dong G. Hydrodynamic forces on dual cylinders of different diameters in steady currents. J Fluid Struct 2007;23:59–83.

[20] Hoerner SF. Fluid-dynamic drag. New York, USA: Practical Information on Aerodynamic Drag and Hydrodynamic Resistance; 1965.

[21] https://www.sintef.no/en/software/simla-pipeline-analysis-tool/.

[22] Orcina. Modelling contact in OrcaFlex. UK: Cumbria; 2018.

[23] Achenbach E, Heinecke E. On vortex shedding from smooth and rough cylinders in the range of Reynolds numbers 6×103 to 5×106. J Fluid Mech 1981;109: 239–51.

[24] Achenbach E. Distribution of local pressure and skin friction around a circular cylinder in cross-flow up to Re = 5×106. J Fluid Mech 1968;34(4):625–39.

[25] Herdiyanti J. Comparisons study of S-lay and J-lay methods for pipeline installation in ultra deep water, master thesis at the department of mechanical and structural engineering and materials science. Stavanger, Norway: University of Stavanger; 2013.